Numerical study of circular double-skin concrete-filled aluminum tubular stub columns

Patel, V. I., Liang, Q. Q. and Hadi, M. N. S. (2019). Numerical study of circular double-skin concrete-filled aluminum tubular stub columns. *Engineering Structures*, 197: 109418

Numerical study of circular double-skin concrete-filled aluminum tubular stub columns

Vipulkumar Ishvarbhai Patel[a], Qing Quan Liang[b,*], Muhammad N. S. Hadi[c]

[a]*School of Engineering and Mathematical Sciences, La Trobe University, Bendigo, VIC 3552, Australia*
[b]*College of Engineering and Science, Victoria University, PO Box 14428, Melbourne, VIC 8001, Australia*
[c]*School of Civil, Mining and Environmental Engineering, University of Wollongong, Wollongong, NSW 2522, Australia*

ABSTRACT

The sandwiched concrete in a circular double-skin concrete-filled aluminum tubular (DCFAT) column is subjected to the lateral confinement from inner and outer aluminum tubes. The effects of double-skin confinement have not been considered in the existing numerical models for the analysis of DCFAT stub columns. This paper describes a numerical model for the simulation of concentrically compressed circular DCFAT short columns. The numerical model is developed using the fiber element methodology. A new expression for determining the lateral confining pressures on the sandwiched concrete in circular DCFAT stub columns is proposed based on experimental results and incorporated in the computational technique. The stress-strain relations for determining the material performance of aluminum and confined sandwiched concrete are described. The numerical model is validated through comparisons with the experimental results of circular DCFAT stub columns. The numerical predictions correlate well with the tested column results, especially the aluminum stress-strain responses, load-strain responses, and ultimate axial load. A parametric study is performed to ascertain the

*Corresponding author. Tel.: 61 3 9919 4134.
E-mail address: Qing.Liang@vu.edu.au (Q. Q. Liang)

influences of geometric and material variables on the behavior of DCFAT stub columns. The numerical results reveal that the use of aluminum instead of steel in a composite column could reduce the column weight by about 22.5%. The comparison of experimental results with the ultimate loads obtained by the design approaches specified in AISC 360-16, Eurocode 4, and Liang's design model indicates that the codified methods generally either underestimate or overestimate the strengths of DCFAT columns, and Liang's design model gives accurate predictions.

Keywords: Concrete-filled aluminum tubes; Computational modeling; Double-skin confinement; Nonlinear analysis.

1. Introduction

Concrete-filled steel tubular (CFST) columns are utilized in modern composite structures because of their distinguishing features including high axial strength, high strain ductility, high elastic stiffness, and high buckling resistance [1]. The circular double-skin concrete-filled steel tubular (DCFST) column is fabricated by concentrically adding a circular hollow tube in a conventional circular CFST column [2-6]. The inner tube in DCFST columns increases the column flexural stiffness and reduces their overall weight. The use of aluminum tubes instead of steel tubes further decreases the weight of DCFST columns. The weight of aluminum is 35% less than that of steel for the same material strength. Aluminum has distinguished advantages over carbon steels, including aesthetic appearance, corrosion resistance, ductility, durability, energy absorption capacity, and ease of maintenance. Aluminum does not change its properties under the temperatures ranging from –80 °C to +300 °C. Aluminum exhibits good ductility at low temperatures, unlike other constructional materials, which increase their brittleness under

the low temperature. The material benefits of aluminum can efficiently be utilized in the construction sector by placing sandwiched concrete at the space between two hollow aluminum tubes, which makes double-skin concrete-filled aluminum tubular (DCFAT) columns [7]. However, the low fire resistance and initial high material cost of aluminum have limited its use in structural members. Figure 1 illustrates the cross-section of a circular DCFAT column.

Researchers have experimentally captured the strength and overall behavior of CFST columns [8-14]. The performance of DCFST column was also investigated by researchers in the past [4, 15-19]. The results revealed that the peak load of a circular DCFST column is 30% higher than the strength sum of the individual three components. The responses of circular and square concrete-filled aluminum tubular (CFAT) stub columns were experimentally examined by Zhou and Young [20, 21]. Zhou and Young [7] performed an experiment on circular DCFAT stub columns under axial load. The dimeter-to-thickness ratio $\left(D_i/t_i\right)$ of the inner aluminum tube was between 16 and 39 while the diameter-to-thickness ratio $\left(D_o/t_o\right)$ of the outer aluminum tube varied from 29 to 60. The concrete compressive strengths were 45 MPa, 70 MPa, and 106 MPa. The experimental observation revealed that the DCFAT stub columns ultimately failed by the aluminum tube local buckling and sandwiched concrete crushing. The results also revealed that increasing the concrete strength results in an increase in the initial stiffness of DCFAT stub columns, but the ductility decreases due to the brittle nature of high-strength concrete.

The nonlinear analysis and design of CFST columns for determining their stiffness, strength, ductility, and overall behavior were reported [22-33]. The structural performance of DCFST columns was numerically investigated by researchers [34-40]. Zhou and Young [7] developed a finite element model using Abaqus software for the analysis of concentrically compressed

circular DCFAT stub columns. The single-skin concrete confinement was considered for the analysis of sandwiched concrete, which was confined by outer and inner aluminum tubes. The measured stress-strain response from the tension test was employed to model the material behavior of aluminum. Liang [38] reported that the double-skin confinement of sandwiched concrete considerably increases the capacity and ductility of DCFST columns. Hu and Su [36], Pagoulatou et al. [37], and Liang [38] pointed out that the double-skin concrete confinement must be considered in the computational study of circular DCFST columns. Therefore, this paper considers the influence of double-skin confinement in the numerical study of concentrically compressed circular DCFAT stub columns.

Numerical investigations on the structural responses of circular DCFAT have been very limited. The double-skin concrete confinement in DCFAT columns was not recognized in the existing computational study [7]. This paper describes a numerical modeling technique for the computational simulation of circular DCFAT stub columns loaded concentrically. The formulation of the modeling technique incorporates the double-skin confinement on concrete. The aluminum material behavior is modeled using the stress-strain relationships given by Abdella [41]. The details of geometric-material parametric effect on the initial stiffness, ultimate load, and ductility index of circular DCFAT columns are presented by means of parametric studies. An equation given by Liang [38] and existing design standards are utilized to quantify the ultimate loads of circular DCFAT columns. The numerical verifications of these design methods are discussed.

2. Formulation of numerical model

2.1. Discretization of DCFAT column cross-section

The nonlinear modeling technique presented in this paper employs the fiber element methodology to discretize the cross-sections of circular DCFAT columns [38, 42-45]. Figure 2 depicts the typical fiber mesh for circular DCFAT column section. The origin of the coordinate system is located at the section centroid. In the simulation, the double-skin aluminum-concrete composite cross-section is first divided into small fibers. The areas and coordinates of fiber elements are then determined. The contribution of each element is summed to obtain the internal axial force in the cross-section of a circular DCFAT column loaded axially as follows:

$$P = \sum_{i=1}^{nao} \sigma_{ao,i} A_{ao,i} + \sum_{j=1}^{nai} \sigma_{ai,j} A_{ai,j} + \sum_{k=1}^{nsc} \sigma_{sc,k} A_{sc,k} \quad (1)$$

in which P represents the axial force of DCFAT column cross-section, $\sigma_{ao,i}$, $\sigma_{ai,j}$ and $\sigma_{sc,k}$ denote the stresses at the outer aluminum, inner aluminum, and sandwiched concrete element, respectively; $A_{ao,i}$, $A_{ai,j}$ and $A_{sc,k}$ are the outer aluminum, inner aluminum, and sandwiched concrete elemental area, respectively and nao, nai and nsc stand for the number of outer aluminum, inner aluminum, and sandwiched concrete element, respectively.

2.2. Axial load-strain analysis

The structural performance of a concentrically loaded circular DCFAT stub column is characterized by its axial load-strain responses. It is assumed that there is no slippage between the outer aluminum tube, inner aluminum tube, and sandwiched concrete, which means that both aluminum tubes and the sandwiched concrete are subjected to the same longitudinal strain. The concrete core and aluminum tubes are simultaneously loaded so that the components of the DCFST column exhibit the same axial strain [46]. The bond between the tubes and concrete is

so small that it does not have a significant effect on the fundamental behavior of DCFST columns.

A strain-driven technique is adapted to generate the load-strain responses of axially compressed circular DCFAT stub columns. In the strain-driven technique, the axial strain is incrementally increased. For a given axial strain, the axial stresses are determined using the aluminum and sandwiched concrete material models, which are given in Sections 2.3 and 2.4. The internal axial force (P) for the given strain is calculated by the integration of stresses over the composite cross-section using Eq. (1). This computational procedure is repeated until the stopping criterion is satisfied. The stopping criterion is specified as that when the axial load falls to $0.5P_{\max}$ or the ultimate concrete strain ε_{cu} is exceeded. The peak load ($P_{\max}$) on the load-strain curve is treated as the ultimate axial load P_u of circular DCFAT stub columns [47].

2.3. Stress-strain relations of aluminum

The sandwiched concrete in a DCFAT column expands laterally under uniform axial compression. The lateral expansion of concrete is restrained by the outer and inner aluminum tubes. The outer aluminum tube is subjected to axial compression and hoop tension while the inner tube is under the axial and hoop compression. Both outer and inner aluminum tubes provide the lateral confining pressure to the sandwiched concrete. The hoop compression and tension developed in the tubes reduces the proof strength of the outer and inner aluminum tubes. This effect is considered in the material stress-strain relations of aluminum tubes by multiplying the factor of 0.9 with the 0.2% proof stress $\sigma_{0.2}$ as shown in Fig. 3.

Figure 3 illustrates the generalized stress-strain responses of aluminum material. The constitutive behavior of aluminum is usually modeled into two stages. The first-stage is defined by the strain from zero to $\varepsilon_{0.2}$, and the second-stage falls in the aluminum strain between $0.9\varepsilon_{0.2}$ and ε_{au}. Ramberg and Osgood [48] proposed an equation for expressing the stress-strain relations of aluminum, in which the strain is calculated from the given stress. The numerical simulation such as fiber element analysis generally requires calculating the stress from the given strain [49]. Abdella [41] proposed the inversion of the stress-strain relationship given by Ramberg and Osgood [48], in which the stress is computed from the given strain. The stress-strain model given by Abdella [41] is implemented in the numerical modeling technique to capture the material performance of aluminum. The stresses in the first-stage of aluminum stress-strain behavior are determined by [41]:

$$\sigma_a = \frac{0.9\sigma_{0.2} r \left(\varepsilon_a / \varepsilon_{0.2}\right)}{1+\left(r-1\right)\left(\varepsilon_a / \varepsilon_{0.2}\right)^p} \tag{2}$$

where σ_a represents the aluminum stress, ε_a is the strain at the stress σ_a, $\sigma_{0.2}$ and $\varepsilon_{0.2}$ denote the 0.2% aluminum proof stress and strain, respectively. The strain $\varepsilon_{0.2}$ is expressed by [48]:

$$\varepsilon_{0.2} = 0.002 + \frac{0.9\sigma_{0.2}}{E_0} \tag{3}$$

in which E_0 denotes the Young's modulus of aluminum. In Eq. (2), r and p are material constants which were proposed by Abdella [41] as

$$r = \frac{E_0 \varepsilon_{0.2}}{0.9\sigma_{0.2}} \tag{4}$$

$$p = \frac{r\left(1-r_2\right)}{r-1} \tag{5}$$

where r_2 is the material constant proposed by Abdella [41]:

$$r_2 = \frac{E_{0.2}\varepsilon_{0.2}}{0.9\sigma_{0.2}} \tag{6}$$

in which $E_{0.2}$ stands for the tangent modulus of aluminum, which is determined using the equation provided by Ramberg and Osgood [48] as

$$E_{0.2} = \frac{E_0}{1+0.002\left(\frac{nE_0}{0.9\sigma_{0.2}}\right)} \tag{7}$$

The aluminum stresses in the second-stage $\left(0.2\varepsilon_{0.2} < \varepsilon_a \le \varepsilon_{au}\right)$ as shown in Fig. 3 are predicted from the given strains [41] as follows:

$$\sigma_a = 0.9\sigma_{0.2}\left[1+\frac{r_2\left(\varepsilon_a/\varepsilon_{0.2}-1\right)}{1+\left(r^*-1\right)\left(\frac{\varepsilon_a/\varepsilon_{0.2}-1}{\varepsilon_{au}/\varepsilon_{0.2}-1}\right)^{p^*}}\right] \tag{8}$$

where r^* and p^* represent the material constants which were given by Abdella [41] as

$$r^* = \frac{E_{0.2}\left(\varepsilon_{au} - \varepsilon_{0.2}\right)}{\left(\sigma_{au} - 0.9\sigma_{0.2}\right)} \tag{9}$$

$$p^* = \frac{r^*\left(1 - r_u\right)}{r^* - 1} \tag{10}$$

in which

$$r_u = \frac{E_u\left(\varepsilon_{au} - \varepsilon_{0.2}\right)}{\sigma_{au} - 0.9\sigma_{0.2}} \tag{11}$$

The slope E_u proposed by Abdella [41] is written as

$$E_u = \frac{E_{0.2}}{1 + \left(r^* - 1\right)m} \tag{12}$$

where m is the stress-strain model parameter given by Rasmussen [50], which is expressed as

$$m = 1 + 3.5\left(\frac{0.9\sigma_{0.2}}{\sigma_{au}}\right) \tag{13}$$

in which σ_{au} represents the aluminum ultimate stress.

2.4. Stress-strain relations of sandwiched concrete

The single-skin confinement models developed for concrete in circular CFST columns may not accurately capture the true performance of double-skin confined sandwiched concrete in

circular DCFAT stub columns. To overcome this problem, the double-skin confinement must be employed in the computational modeling of circular DCFAT stub columns. The stress-strain relationship shown in Fig. 4 given by Liang [38] is employed in the present computational method to capture the confinement characteristics of sandwiched concrete in circular DCFAT columns. The parabolic ascending branch OA of the concrete stress-strain relation is simulated using the following equation given by Mander et al. [51] for double-tube confined concrete:

$$\sigma_c = \frac{f_{cc}^{'}\lambda\left(\varepsilon_c/\varepsilon_{cc}^{'}\right)}{\lambda-1+\left(\varepsilon_c/\varepsilon_{cc}^{'}\right)^{\lambda}} \tag{14}$$

$$\lambda = \frac{E_c}{E_c-\left(f_{cc}^{'}/\varepsilon_{cc}^{'}\right)} \tag{15}$$

where σ_c and ε_c denote the compressive concrete stress and strain, respectively, $f_{cc}^{'}$ and $\varepsilon_{cc}^{'}$ represent the compressive strength and strain of double-skin confined concrete, λ is the material constant of sandwiched concrete, and E_c represents Young's modulus of sandwiched concrete which is determined by [52]

$$E_c = 3320\sqrt{\gamma_c f_c^{'}} + 6900 \quad (\text{MPa}) \tag{16}$$

where $f_c^{'}$ denotes the concrete cylinder compressive strength, γ_c represents the strength reduction factor which considers the influence of concrete quality, loading rate, and column size on the concrete cylinder strength $f_c^{'}$. The parameter γ_c was modified by Liang [38] for a circular DCFST column based on the equation proposed by Liang [44] for a conventional CFST column as

$$\gamma_c = 1.85 t_c^{-0.135} \quad \left(0.85 \le \gamma_c \le 1.0\right) \tag{17}$$

where t_c represents the sandwiched concrete thickness as depicted in Fig. 1, and is computed by

$$t_c = \frac{D_o}{2} - t_o - \frac{D_i}{2} \tag{18}$$

in which D_o and t_o denote the outer aluminum tube diameter and thickness, respectively and D_i represents the inner aluminum tube diameter as illustrated in Fig. 1.

In Eq. (14), the compressive strength $\left(f_{cc}^{'}\right)$ of double-skin confined concrete and the corresponding strain $\left(\varepsilon_{cc}^{'}\right)$ are obtained by using the equation given by Mander et al. [51] with the factor γ_c. Liang [38] modified the equations given by Mander et al. [51] for predicting the confined sandwiched concrete strength $\left(f_{cc}^{'}\right)$ and strain $\left(\varepsilon_{cc}^{'}\right)$ as follows:

$$f_{cc}^{'} = \gamma_c f_c^{'} + 4.1 f_{rp} \tag{19}$$

$$\varepsilon_{cc}^{'} = \varepsilon_c^{'}\left(1 + 20.5\frac{f_{rp}}{\gamma_c f_c^{'}}\right) \tag{20}$$

Note that the compressive strength $\left(f_{cc}^{'}\right)$ and strain $\left(\varepsilon_{cc}^{'}\right)$ depend on the confining pressure $\left(f_{rp}\right)$ of the double-skin sandwiched concrete. In Eq. (20), the unconfined concrete strain $\varepsilon_c^{'}$ at the stress $f_c^{'}$ is determined using the equation proposed by Liang [44] as follows:

$$\varepsilon_c^{'} = \begin{cases} 0.002 & \text{for } \gamma_c f_c^{'} \le 28(\text{MPa}) \\ 0.002 + \dfrac{\gamma_c f_c^{'} - 28}{54,000} & \text{for } 28 < \gamma_c f_c^{'} \le 82(\text{MPa}) \\ 0.003 & \text{for } \gamma_c f_c^{'} > 82(\text{MPa}) \end{cases} \tag{21}$$

In Eq. (19), the lateral confining pressure $\left(f_{rp}\right)$ on the sandwiched concrete accounts for the effect of the confinement exerted by both inner and outer aluminum tubes. The lateral confining pressure f_{rp} depends on the diameter-to-thickness ratios of the inner and outer tubes. The stress contributions of sandwiched concrete to the ultimate axial strength of DCFAT columns were calculated from the experimental results given by Zhou and Young [7]. The regression analysis as shown in Fig. 5 was conducted to estimate the lateral confining pressure f_{rp} using the experimental stress contribution of sandwiched concrete. The proposed equation is given as:

$$f_{rp} = 10.0445 - 0.3090\left(\frac{D_o}{t_o}\right) - 0.0417\left(\frac{D_i}{t_i}\right) + 0.0025\left(\frac{D_o}{t_o}\right)^2 + 0.0014\left(\frac{D_o}{t_o}\right)\left(\frac{D_i}{t_i}\right) - 0.001\left(\frac{D_i}{t_i}\right)^2 \tag{22}$$

in which t_i denotes the inner aluminum tube thickness as illustrated in Fig. 1, and $f_{rp} \ge 0$. Equation (22) applies to columns with $D_o / t_o \le 60$ and $D_i / t_i \le 40$. The lateral confining pressure on the sandwiched concrete is zero when the inner diameter-to-thickness ratio $D_i / t_i \ge 40$.

The linear branches AB and BC of the concrete stress-strain relationship illustrated in Fig. 4 are determined using the following equations:

$$\sigma_c = \begin{cases} \beta_c f_{cc}^{'} + \left(f_{cc}^{'} - \beta_c f_{cc}^{'} \right) \left(\dfrac{\varepsilon_{cu} - \varepsilon_c}{\varepsilon_{cu} - \varepsilon_{cc}^{'}} \right) & \text{for } \varepsilon_{cc}^{'} < \varepsilon_c \le \varepsilon_{cu} \\ \beta_c f_{cc}^{'} & \text{for } \varepsilon_c > \varepsilon_{cu} \end{cases} \tag{23}$$

where β_c represents the material degradation factor, which determines the residual strength and strain ductility of the confined sandwiched concrete in the post-yield region. The equations proposed by Liang [38] are employed in the fiber-based numerical study, express by

$$\beta_c = \begin{cases} 1.0 & \text{for } D_o/t_o \le 40 \\ k_3 & \text{for } D_o/t_o > 40 \\ 0.0000339\left(D_o/t_o\right)^2 - 0.010085\left(D_o/t_o\right) + 1.349 & \text{for } k_3 < 0 \end{cases} \tag{24}$$

in which k_3 was proposed by Hu and Su [36] as

$$\begin{aligned} k_3 = {} & 1.73916 - 0.00862\left(\frac{D_o}{t_o}\right) - 0.04731\left(\frac{D_i}{t_i}\right) - 0.00036\left(\frac{D_o}{t_o}\right)^2 \\ & + 0.00134\left(\frac{D_o}{t_o}\right)\left(\frac{D_i}{t_i}\right) - 0.00058\left(\frac{D_i}{t_i}\right)^2 \ge 0 \end{aligned} \tag{25}$$

In Eq. (23), the strain ε_{cu} was proposed by Liang [38], which is expressed by

$$\varepsilon_{cu} = \begin{cases} 0.03 & \text{for } D_o / t_o \le 60 \\ 0.023 + 0.000175(100 - D_o / t_o) & \text{for } 60 < D_o / t_o \le 100 \\ 0.02 & \text{for } D_o / t_o > 100 \end{cases} \tag{26}$$

3. Verification of the numerical model

3.1. Stress-strain relationships of aluminum

The accuracy of the material model given by Abdella [41] for modeling the material behavior of aluminum was assessed. The predicted stress-strain responses of aluminum using equations presented in Section 2.3 are compared with the measured ones given by Zhou and Young [7]. The material parameters of aluminum are listed in Table 1. The nonlinearity index (n) was not given by Zhou and Young [7] so that it was assumed to be 5.0. Figure 7 demonstrates the comparison of the computed and experimentally observed stress-strain performance for Specimens C4 and CHS2. It is found that the fiber-based method of analysis accurately estimates the overall trend of the stress-strain responses of aluminum. The measured elastic responses of aluminum are well captured by the numerical model. The model also simulates well the aluminum post-yield behavior. The verification indicates that the stress-strain relationship given by Abdella [41] based on Ramberg-Osgood equation [48] can be incorporated in the numerical simulation of circular DCFAT stub columns.

3.2. Ultimate axial load

The experimental results provided by Zhou and Young [7] were employed to validate the numerical model developed. Table 2 provides the geometric parameters and material details of tested DCFAT stub columns. In Table 2, $P_{u\exp}$ stands for the experimental ultimate load, $P_{u\mathrm{num}}$ is the numerical ultimate load, $\sigma_{0.2o}$ represents the 0.2% proof stress of outer aluminum tube, σ_{auo} denotes the ultimate strength of outer aluminum tube, E_{0o} stands for Young's modulus of outer aluminum tube, $\sigma_{0.2i}$ represents the 0.2% proof stress of inner aluminum tube, σ_{aui}

denotes the ultimate strength of inner aluminum tube, and E_{0i} represents Young's modulus of inner aluminum tube. In general, the predicted ultimate axial loads correlate well with experimental values, and the discrepancy is within 10%, which is acceptable for engineering design purpose. The mean computational-to-test ultimate load ratio is 1.020 with a standard deviation (SD) of 0.050 and a coefficient of variation (COV) of 0.050. The verification given in Table 2 indicates that the computational model reasonably quantifies the ultimate load of axially compressed circular DCFAT stub columns.

Table 3 presents the comparison of the lateral confining pressures provided by the carbon steel tube and aluminum tube on the sandwiched concrete. The confinement model given by Hu and Su [36] was utilized for determining the lateral pressures on the sandwiched concrete in circular steel tubes. The lateral pressures in DCFAT columns were calculated by the proposed Eq. (22). It is found that the lateral confining pressures by carbon steel tube are generally higher than those by aluminum tube. This is because the initial stiffness of the carbon steel is three times higher than that of the aluminum. It can be seen from Table 3 that the ultimate axial strengths of DCFAT columns may be overestimated by using the confinement model based on the carbon steel tubes.

3.3. Load-strain behavior

Figure 7 depicts the comparison of load-strain responses of Specimens C5C1-C40 and C5C1-C70 tested by Zhou and Young [7]. As depicted in Fig. 7, the numerical model closely estimates the load-strain relationships of axially compressed circular DCFAT stub columns. Nevertheless, there is a small discrepancy between numerical and test data for Specimen C5C1-C40 after attending the 800 kN axial load. For Specimen C5C1-C70, the predicted axial

stiffness and post-peak response deviate slightly from experimental data. This is because of the uncertainty of sandwiched concrete strength used in the numerical simulation. It can be concluded that the numerical modeling technique reasonably simulates the load-strain responses of circular DCFAT stub columns.

4. Parametric study

Following the verification study discussed in Section 3, the influences of material strength and geometric variables on the load-strain performance, axial capacity, and strain ductility of circular DCFAT stub columns were examined. The design parameters included the inner tube diameter-to-outer tube diameter D_i/D_o ratio, outer tube diameter-to-thickness D_o/t_o ratio, inner tube diameter-to-thickness D_i/t_i ratio, sandwiched concrete strength and aluminum strength. Table 4 summarizes the dimension and material variables for the parametric study. The Young's modulus of both outer and inner aluminum tubes was taken as 69 GPa in the parametric study. The nonlinearity index (n) of aluminum was assumed to be 5.0. The strain ductility of a DCFAT column was calculated using the strain ratio given by Liang [38]:

$$PI_{sd} = \frac{\varepsilon_u}{\varepsilon_y} \tag{27}$$

$$\varepsilon_y = \frac{\varepsilon_{0.75}}{0.75} \tag{28}$$

in which ε_u denotes the longitudinal axial strain of DCFAT column at the 90% ultimate axial load in the descending regime, $\varepsilon_{0.75}$ stands for the axial strain at the 75% ultimate load in the

pre-peak regime. For the load-strain relation with strain-hardening behavior, the axial strain ε_u is equal to the ultimate axial strain, which is specified as 0.04 in the analyses.

4.1. Comparison of DCFAT and DCFST columns

The fiber analyses were carried out to quantify the load-strain relations of circular DCFAT and DCFST columns with the same dimensions and material strengths. For DCFST columns, the fiber model proposed by Liang [38] was used to calculate the load-strain responses. Column C1 listed in Table 4 was modeled to compare the load-strain performance of circular DCFAT and DCFST columns. Figure 8 presents the comparison of the load-strain relations for DCFAT and DCFST columns. As appeared, the initial stiffness and ultimate axial strength of the DCFST stub column are higher than that of the DCFAT stub column. This is explained by the fact that the elastic modulus of carbon steel (200 GPa) is higher than that of aluminum (69 GPa). The reason for the higher ultimate strength is that the confinement provided by the steel tube is higher than that by the aluminum tube. The post-peak behavior of load-strain curves indicates that the DCFAT column exhibits higher ductility than DCFST column. This is because the ductility of aluminum in compression is higher than that of carbon steel.

4.2. Effect of D_i/D_o ratio

The ultimate axial strength and strain ductility of circular DCFAT stub columns are affected by the D_i/D_o ratio. Columns C2-C5 given in Table 4 were numerically analyzed. As shown in Table 4, the D_i/D_o ratios were calculated by means of changing the inner aluminum tube diameter D_i for the same outer aluminum tube diameter D_o. Figure 9 presents the effect of

D_i/D_o ratio on the load-strain responses of circular DCFAT columns. The results illustrate that the change in D_i/D_o ratio has a slight influence on the elastic stiffness, but the peak load decreases considerably as D_i/D_o ratio increases. The reason for this is that the increase in the D_i/D_o ratio reduces the sandwiched-concrete area so that the column ultimate load decreases. As the D_i/D_o ratio increases from 0.3, 0.4, 0.5 and 0.6, the percentage reduction in the column ultimate load is 3.2%, 12.3% and 17.4%, respectively. Figure 10 illustrates the D_i/D_o ratio-ductility relationship of circular DCFAT stub columns. As appeared in Fig. 10, changing the D_i/D_o ratio from 0.3 to 0.5 results in an increase in the strain ductility index. However, when the D_i/D_o ratio is greater than 0.5, the strain ductility index PI_{sd} decreases when the D_i/D_o ratio increases. This is attributed to the fact that the double-skin confining pressure reduces because of the increase in the D_i/D_o or D_i/D_o ratio. Liang [38] found that the confining pressure is equal to zero when $D_i/t_i \geq 40$. Tao et al. [16] reported the similar ductility behavior for the influence of D_i/D_o ratio of circular DCFST stub columns. It is recommended that the D_i/D_o ratio should be maintained less than 0.5 for the good ductility of circular DCFAT columns.

4.3. Effect of D_o/t_o ratio

The structural features of circular DCFST columns could be effectively improved by increasing the outer tube diameter instead of outer tube thickness for the same D_o/t_o ratio [38]. The different D_o/t_o ratios were obtained by changing the outer aluminum tube diameter D_o for the same thickness t_o. The computer modeling approach proposed was utilized to simulate Columns C6, C7, and C8 given in Table 4 for examining the influences of D_o/t_o ratio on the

performance of circular DCFAT columns. Figure 11 shows the effect of D_o/t_o ratio on the load-strain relations of circular DCFAT columns. The computational results indicate that increasing the outer aluminum tube diameter noticeably increases the elastic stiffness and sustainably improves the peak load of circular DCFAT columns. This is because increasing the outer-tube diameter increases the cross-sectional area of the column. When the D_o/t_o ratio is changed from 45 to 55 and 60, the ultimate load increases by 41.5% and 65.5%, respectively. The relationship between strain ductility index PI_{sd} and D_o/t_o ratio for circular DCFAT columns is depicted in Fig. 12. As demonstrated, the strain ductility PI_{sd} considerably decreases with an increase in D_o/t_o ratio. The ductility index PI_{sd} is 5.97 for the D_o/t_o ratio of 45, but it reduces to 5.58 and 5.16 as the D_o/t_o ratio changes from 45 to 55 and 60, respectively.

4.4. Effect of D_i/t_i ratio

The influences of D_i/t_i ratio on the behavior of circular DCFAT stub columns were investigated by employing the fiber-based computational procedure. The different D_i/t_i ratios were calculated by altering the tube thickness while the tube diameter was not changed. Analyses on Columns C9, C10, and C11 given in Table 4 were carried out using the computational model. The computed load-strain relations of the DCFAT columns with various D_i/t_i ratios are shown in Fig. 13. The peak load decreases markedly with increasing the D_i/t_i ratio. As the D_i/t_i ratio changes from 15 to 25 and 35, the column ultimate load decreases by 4.63% and 8.54%, respectively. Note that changing the D_i/t_i ratio has a negligible influence on the elastic stiffness of these columns as shown in Fig. 13. The effect of D_i/t_i ratio on the

ductility index PI_{sd} of circular DCFAT columns is demonstrated in Fig. 14. The strain ductility PI_{sd} is found to slightly decrease when the D_i/t_i ratio increases. For the D_i/t_i ratios of 15, 25 and 35, the strain ductility indices are 6.34, 5.78 and 4.88, respectively.

4.5. Effect of aluminum proof stress

The double-skin aluminum tubes provide confining pressures to the sandwiched concrete in a circular DCFAT column under concentric loading. The double-skin confinement in circular DCFAT column increases both the ductility and compressive strength of sandwiched concrete. The behavior of DCFAT columns was examined by varying the aluminum proof stress of Columns C12 to C15 listed in Table 4. Figure 15 gives the load-strain performance of circular DCFAT columns with different aluminum proof stresses. It can be observed that the change of aluminum proof stress has a negligible influence on the elastic stiffness, but the ultimate load slightly increases as the aluminum proof stress increases. Because of changing the aluminum proof stress from 220 MPa to 260 MPa, the column peak load increases by 5.99%. However, the strain ductility index does not change with increasing the proof stress as depicted in Fig. 16. The numerical results reveal that the aluminum proof stress of 260 MPa or greater than 260 MPa should be utilized to improve the axial compression capacity of circular DCFAT columns.

4.6. Effect of concrete strength

The influence of concrete compressive strength on the characteristics of circular DCFAT stub columns was studied. Columns C16 to C19 given in Table 4 were analyzed for this purpose. The load-strain responses of the DCFAT stub columns with various concrete strengths are provided in Fig. 17. The use of higher strength concrete results in a noticeable increase in the

column initial axial stiffness, but a remarkable improvement in its ultimate load. When changing the concrete strength of 40 MPa to 65 MPa, 80 MPa, and 100 MPa, the peak load increases by 31.31%, 50.49%, and 75.74%, respectively. However, as illustrated in Fig. 18, the higher the concrete compressive strength, the lower the strain ductility. The strain ductility indices PI_{sd} of circular DCFAT stub columns filled with 40 MPa, 65 MPa, 80 MPa, and 100 MPa concrete are 7.35, 6.01, 5.37 and 4.85, respectively.

4.7. Comparison of column weights

Pagoulatou et al. [37] presented the weight comparison of circular CFST and DCFST stub columns. It was found that a circular DCFST column was 30% lighter than the equivalent circular CFST column. The parametric study was performed to conduct the weight comparison of circular DCFST and DCFAT stub columns. The dimensions of Column C20 in Table 4 were utilized to calculate the volume of three components. The length of Column C20 was 900 mm. The AS/NZS 1170.1 [53] gives the density of structural materials for determining the permanent action. The density of aluminum, unreinforced concrete, and steel is 26.7 kN/m^3, 24.0 kN/m^3, and 76.9 kN/m^3, respectively. The weight of a circular DCFST column is calculated as 159.7 kg while a circular DCFAT column is weighed 123.7 kg. It can be concluded that the use of aluminum instead of carbon steel in composite columns reduces the column weight by 22.5%.

5. Design of circular DCFAT stub columns

5.1. General

The existing design standards do not recommend the methods for quantifying the ultimate axial loads of circular DCFAT stub columns. Therefore, the design provisions given in the current structural design standards for circular CFST stub columns were used to evaluate their applicability to the design of circular DCFAT stub columns.

5.2. AISC 316-16

The design approach reported in AISC 316-16 [54] for estimating the ultimate axial load of circular CFST columns does not consider the confinement induced by the tubes. The ultimate load is computed by adding the component strengths of tube and concrete. The design equation given by AISC 316-16 [54] for circular CFST columns is modified for circular DCFAT columns as

$$P_{u.\mathrm{AISC}} = A_{ai}\sigma_{0.2i} + A_{ao}\sigma_{0.2o} + 0.95 f_c^{'} A_{sc} \tag{29}$$

in which A_{ai}, A_{ao}, and A_{sc} stand for the cross-sectional area of the internal aluminum tube, outer aluminum tube, and sandwiched concrete, respectively.

5.3. Eurocode 4

Eurocode 4 [55] provision considers the concrete confinement for computing the ultimate load of circular CFST columns. The provision for circular CFST columns is modified by incorporating the ultimate strengths of inner and outer aluminum tubes for circular DCFAT columns. Based on Eurocode 4 [55], the ultimate load of a concentrically compressed circular DCFAT stub column is calculated by

$$P_{u.\mathrm{EC4}} = \eta_a A_{ai}\sigma_{0.2i} + \eta_a A_{ao}\sigma_{0.2o} + A_{sc} f_c^{'}\left(1+\eta_c \frac{t_o}{D_o}\frac{\sigma_{0.2o}}{f_c^{'}}\right) \tag{30}$$

Note that the Eurocode 4 [55] does not consider the double-skin confinement. Therefore, the confinement induced by an outer aluminum tube is considered in Eq. (30). The parameters η_a and η_c expressing the confinement effect are given as

$$\eta_a = 0.25\left(3+2\overline{\lambda}\right) \qquad \eta_a \le 1 \tag{31}$$

$$\eta_c = 4.9 - 18.5\overline{\lambda} + 17\overline{\lambda}^2 \qquad \eta_c \ge 0 \tag{32}$$

where $\overline{\lambda}$ denotes the slenderness of the DCFAT column, which is defined by

$$\overline{\lambda} = \sqrt{\frac{N_{pl.Rk}}{N_{cr}}} \tag{33}$$

in which $N_{pl.Rk}$ represents the plastic strength of the cross-section, which is determined as

$$N_{pl.Rk} = A_{ai}\sigma_{0.2i} + A_{ao}\sigma_{0.2o} + f_c^{'}A_{sc} \tag{36}$$

In Eq. (33), N_{cr} stands for the Euler buckling load of pin-ended DCFAT column, which is written as

$$N_{cr} = \frac{\pi^2 \left(EI\right)_{eff}}{L^2} \tag{37}$$

in which L represents the effective length of a circular DCFAT column, and $(EI)_{eff}$ denotes the effective bending stiffness of a DCFAT column, which can be expressed by

$$(EI)_{eff} = E_{0i}I_{ai} + E_{0o}I_{ao} + 0.6E_{cm}I_{sc} \tag{38}$$

in which I_{ai}, I_{ao} and I_{sc} stand for the second moment of area of the inner aluminum tube, outer aluminum tube, and sandwiched concrete, respectively, and E_{cm} denotes Young's modulus of elasticity for sandwiched concrete, which is obtained using

$$E_{cm} = 22000\left(\frac{f_c^{'}+8}{10}\right)^{0.3} \tag{39}$$

5.4. Design model by Liang

Liang [38] proposed an equation for determining the ultimate load of concentrically compressed circular DCFST stub columns. Liang's equation [38] considers the influence of double-skin confinement in the design of DCFST columns and is expressed as

$$P_{u\text{Liang}} = \gamma_{ai}\sigma_{0.2i}A_{ai} + \gamma_{ao}\sigma_{0.2o}A_{ao} + \left(\gamma_c f_c^{'} + 4.1 f_{rp}\right)A_{sc} \tag{40}$$

in which γ_c and f_{rp} are determined using Eqs. (17) and (22), respectively. The fiber model has been used to compute the stress contributions of the outer and inner aluminum tubes in tested specimens [7] to the ultimate axial strength of DCFAT columns. The regression analysis has

been conducted on the stress contributions to estimate the strength factors γ_{ai} and γ_{ao}. These factors, γ_{ai} and γ_{ao}, are proposed as follows:

$$\gamma_{ai} = 0.7451\left(\frac{D_i}{t_i}\right)^{-0.022} \tag{41}$$

$$\gamma_{ao} = 2.8548\left(\frac{D_o}{t_o}\right)^{-0.311} \tag{42}$$

5.5. Comparison of test results with existing design standards and model

The ultimate loads of circular DCFAT columns tested by Zhou and Young [7] are compared to those predicted by all the above design standards and model in Table 5, where P_u represents the ultimate axial load of the DCFAT short columns obtained from experiments. The mean of the ultimate loads obtained from the design methods given in AISC 316-16 [54] to the experimental and numerical values is 0.999 with an SD of 0.063 and COV of 0.063. This implies that the approach specified in AISC 316-16 [54] slightly underestimates the ultimate loads of circular DCFAT columns. This is because the design rules provided in AISC 316-16 [54] do not account for the influence of double tube concrete confinement. On the other hand, the design specifications in Eurocode 4 [55] overestimate the ultimate loads of circular DCFAT stub columns. The statistical mean value of code-to-experimental and numerical ultimate load ratio is 1.076 with an SD of 0.064 and COV of 0.059. The design equation given by Liang [38] considers the effect of double-skin confinement in the design of circular DCFST columns. Liang's design equation [38] closely estimates the ultimate load of circular DCFAT columns. The mean computed-to-test ultimate load ratio is 0.986 with an SD of 0.039 and COV of 0.039.

6. Conclusions

The fiber-based computational modeling method has been presented in this paper that simulates the behavior of circular DCFAT stub columns loaded concentrically. A new model for predicting the lateral confining pressures on the sandwiched concrete confined by circular aluminum tubes has been proposed. The computational method has incorporated accurate stress-strain models not only for aluminum but also for sandwiched concrete confined by double-skins. The formulation of the computer simulation method and modeling procedure for accurately modeling the axial load-strain responses of DCFAT stub columns have been described. The comparisons with experimental data have demonstrated that the computer modeling procedure using fiber approach accurately quantifying the behavior of DCFAT stub columns. It has been found that the lateral pressure on the sandwiched concrete provided by the carbon steel tubes is higher than that by the aluminum tubes.

For columns with the same dimensions and material strengths, DCFAT columns have lower initial stiffness, the same ultimate strength, and little higher post-peak axial loads than DCFST columns. The ultimate axial load of circular DCFAT columns is found to increase remarkably with an increase in the D_o/t_o ratio, aluminum proof stress, and concrete strength. In contrast, the ultimate axial load is decreased by increasing the D_i/D_o ratio, and D_i/t_i ratio. The ductility of circular DCFAT columns reduces with an increase in D_o/t_o ratio, concrete strength and aluminum strength, and it increases with increasing the D_i/t_i ratio. The weight of a circular DCFAT column is 22.5% lower than that of the equivalent circular DCFST column. The design provisions given in AISC 316-16 [54] and Eurocode 4 [55] either underestimate or overestimate the axial load-carrying capacities of circular DCFAT stub columns. Liang's design equation

accounting for the double-tube confinement yields accurate estimations of the ultimate axial loads of short circular DCFAT columns.

References

[1] Patel VI, Liang QQ, and Hadi MNS. Concrete-filled stainless steel tubular columns. Boca Raton and London: CRC Press, Taylor and Francis, 2018.

[2] Wright HD, Oduyemi TOS, Evans HR. The experimental behavior of double skin composite elements. J Constr Steel Res 1991;19(2):97-110.

[3] Wright HD, Oduyemi TOS, Evans HR. The design of double skin composite elements. J Constr Steel Res 1991;19(2):111-32.

[4] Wei S, Mau ST, Vipulanandan C, Mantrala SK. Performance of new sandwich tube under axial loading: experiment. J Struct Eng, ASCE 1995;121(12):1806-14.

[5] Liang QQ, Uy B, Wright HD, Bradford MA. Local and post-local buckling of double skin composite panels. Struct Build, Proc Inst Civ Eng, UK 2003;156(2):111-9.

[6] Liang QQ, Uy B, Wright HD, Bradford MA. Local buckling of steel plates in double skin composite panels under biaxial compression and shear. J Struct Eng, ASCE 2004;130(3):443-51.

[7] Zhou F, Young B. Concrete-filled double-skin aluminum circular hollow section stub columns. Thin-Walled Struct 2018;133:141-52.

[8] O'Shea MD, Bridge RQ. Design of circular thin-walled concrete filled steel tubes. J Struct Eng, ASCE 2000;126:1295-1303.

[9] Sakino K, Nakahara H, Morino S, Nishiyama I. Behavior of centrally loaded concrete-filled steel-tube short columns. J Struct Eng, ASCE 2004;130:180-88.

[10] Giakoumelis G, Lam D. Axial capacity of circular concrete-filled tube columns. J Constr Steel Res 2004;60:1049-68.

[11] Young B, Ellobody E. Experimental investigation of concrete-filled cold-formed high strength stainless steel tube columns. J Constr Steel Res 2006;62:484-92.

[12] Uy B, Tao Z, Han LH. Behaviour of short and slender concrete-filled stainless steel tubular columns. J Constr Steel Res 2011;67:360-78.

[13] Han LH, Li W, Bjorhovde R. Development and advanced applications of concrete-filled steel tubular (CFST) structures: Members. J Constr Steel Res 2014;100:211-28.

[14] Liew JYR, Xiong MX, Xiong DX. Design of concrete filled tubular beam-columns with high strength steel and concrete. Structures 2016;8:213-26.

[15] Zhao XL, Grzebieta R, Elchalakan M. Tests of concrete-filled double skin CHS composite stub columns. Steel Compos Struct 2002;2(2):129-46.

[16] Tao Z, Han LH, Zhao XL. Behavior of concrete-filled double skin (CHS inner and CHS outer) steel tubular stub columns and beam-columns. J Constr Steel Res 2004;60:1129-58.

[17] Han LH, Huang H, Tao Z, Zhao XL. Concrete-filled double skin steel tubular (CFDST) beam-columns subjected to cyclic bending. Eng Struct 2006;28(12):1698-714.

[18] Uenaka K, Kitoh H, Sonoda K. Concrete filled double skin circular stub columns under compression. Thin-Walled Struct 2010;48:19-24.

[19] Elchalakani M, Hassanein MF, Karrech A, Fawzia S, Yang B, Patel VI. Experimental tests and design of rubberised concrete-filled double skin circular tubular short columns. Structures 2018;15:196-210.

[20] Zhou F, Young B. Tests of concrete-filled aluminum stub columns. Thin-Walled Struct 2008;46:573-583.

[21] Zhou F, Young B. Concrete-filled aluminum circular hollow section column tests. Thin-Walled Struct 2009;47:1272-1280.

[22] Schneider SP. Axially loaded concrete-filled steel tubes. J Struct Eng, ASCE 1998;124(10):1125-38.

[23] Hajjar JF, Schiller PH, Molodan A. A distributed plasticity model for concrete-filled steel tube beam-columns with interlayer slip. Eng Struct 1998;20(8):663-76.

[24] Susantha KAS, Ge HB, Usami T. Uniaxial stress-strain relationship of concrete confined by various shaped steel tubes. Eng Struct 2001;23(10):1331-47.

[25] Shanmugam NE, Lakshmi B, Uy B. An analytical model for thin-walled steel box columns with concrete in-fill. Eng Struct 2002;24(6):825-38.

[26] Hu HT, Huang CS, Wu MH, Wu YM. Nonlinear analysis of axially loaded concrete-filled tube columns with confinement effect. J Struct Eng, ASCE 2003;129(10):1322-9.

[27] Ellobody E, Young B, Lam D. Behaviour of normal and high strength concrete-filled compact steel tube circular stub columns. J Constr Steel Res 2006;62:706-15.

[28] Hatzigeorgiou GD. Numerical model for the behavior and capacity of circular CFT columns, Part I: theory. Eng Struct 2008;30(6):1573-8.

[29] Liang QQ, Fragomeni S. Nonlinear analysis of circular concrete-filled steel tubular short columns under axial loading. J Constr Steel Res 2009;65:2186-96.

[30] Portolés JM, Romero ML, Filippou FC, Bonet JL. Simulation and design recommendations of eccentrically loaded slender concrete-filled tubular columns. Eng Struct 2011;33(5):1576-93.

[31] Tao Z, Wang ZB, Yu Q. Finite element modelling of concrete-filled steel stub columns under axial compression. J Constr Steel Res 2013;89:121-31.

[32] Hassanein MF, Kharoob OF, Liang QQ. Behaviour of circular concrete-filled lean duplex stainless steel-carbon steel tubular short columns. Eng Struct 2013;56:83-94.

[33] Wang ZB, Tao Z, Han LH, Uy B, Lam D, Kang WH. Strength, stiffness and ductility of concrete-filled steel columns under axial compression. Eng Struct 2017;135:209-21.

[34] Wei S, Mau ST, Vipulanandan C, Mantrala SK. Performance of new sandwich tube under axial loading: analysis. J Struct Eng, ASCE 1995;121(12):1815-21.

[35] Huang H, Han LH, Tao Z, Zhao XL. Analytical behavior of concrete-filled double skin steel tubular (CFDST) stub columns. J Constr Steel Res 2010;66:542-55.

[36] Hu HT, Su FC. Nonlinear analysis of short concrete-filled double skin tube columns subjected to axial compressive forces. Mar Struct 2011;24:319-37.

[37] Pagoulatou M, Sheehan T, Dai XH, Lam D. Finite element analysis on the capacity of circular concrete-filled double-skin steel tubular (CFDST) stub columns. Eng Struct 2014;72:102-12.

[38] Liang QQ. Nonlinear analysis of circular double-skin concrete-filled steel tubular columns under axial compression. Eng Struct 2017;131:639-50.

[39] Liang QQ. Numerical simulation of high strength circular double-skin concrete-filled steel tubular slender columns. Eng Struct 2018;168:205-17.

[40] Ahmed M, Liang QQ, Patel VI, Hadi MNS. Nonlinear analysis of rectangular concrete-filled double steel tubular short columns incorporating local buckling. Eng Struct 2018;175:13-26.

[41] Abdella K. Inversion of a full-range stress-strain relation for stainless steel alloys. International Journal of Non-Linear Mechanics 2006;41(3):456-463.

[42] El-Tawil S, Sanz-picón CF, Deierlein GG. Evaluation of ACI 318 and AISC (LRFD) strength provisions for composite beam-columns. J Constr Steel Res 1995;34(1):103-26.

[43] Hajjar JF, Gourley BC. Representation of concrete-filled steel tube cross-section strength. J Struct Eng, ASCE 1996;122(11):1327-36.

[44] Liang QQ. Performance-based analysis of concrete-filled steel tubular beam-columns. Part I: Theory and algorithms. J Constr Steel Res 2009;65(2):363-72.

[45] Liang QQ. Performance-based analysis of concrete-filled steel tubular beam-columns, Part II: Verification and applications. J Constr Steel Res 2009;65(2):351-62.

[46] Kilpatrick AE, Rangan BV. Influence of interfacial shear transfer on behaviour of concrete-filled steel tubular columns. ACI Struct J 1999;96(4):642-48.

[47] Liang QQ. Analysis and Design of Steel and Composite Structures. Boca Raton and London: CRC Press, Taylor and Francis Group, 2014.

[48] Ramberg W, Osgood WR. NACA Technical Note No. 902, 1943.

[49] Patel VI, Liang QQ, Hadi MNS. Nonlinear analysis of axially loaded circular concrete-filled stainless steel tubular short columns. J Constr Steel Res 2014;101:9-18.

[50] Rasmussen KJR. Full-range stress-strain curves for stainless steel alloys. J Constr Steel Res 2003; 59(1): 47-61.

[51] Mander JB, Priestly MNJ, Park R. Theoretical stress-strain model for confined concrete. J Struct Eng, ASCE 1988;114(8):1804-26.

[52] ACI-318-11. Building code requirements for reinforced concrete. ACI Committee 318, Detroit (MI);2011.

[53] AS/NZS 1170.1:2002. Structural design actions Part 1: Permanent, imposed and other actions, Sydney, New South Wales, Australia: Standards Australia; 2002.

[54] AISC 360-16. Specification for Structural Steel Buildings. Chicago (IL, USA): American Institute of Steel Construction; 2016.

[55] EN 1994-1-1. Eurocode 4 - design of composite steel and concrete structures, part 1.1: general rules and rules for building. London (UK): British Standards Institution; 2004.

Figures and tables

Table 1 Material properties of aluminum.

Specimens	$\sigma_{0.2}$ (MPa)	σ_{au} (MPa)	E_0 (GPa)	n	Ref.
C4	267.9	282.9	64.9	5.0	[7]
CHS2	238.4	259.1	66.1	5.0	

Table 2 Ultimate axial loads of circular DCFAT stub columns under axial compression.

Specimens	$D_o \times t_o$ (mm)	$D_i \times t_i$ (mm)	$f_c^{'}$ (MPa)	$\sigma_{0.2o}$ (MPa)	σ_{auo} (MPa)	E_{0o} (GPa)	$\sigma_{0.2i}$ (MPa)	σ_{aui} (MPa)	E_{0i} (GPa)	$P_{u\exp}$ (kN)	$P_{u\text{num}}$ (kN)	$\frac{P_{u\text{num}}}{P_{u\exp}}$	Ref.
C3C1-C40	120.0×2.48	50.0×3.09	44.8	253.1	264.7	66.5	238.4	259.1	66.1	712.4	717.0	1.007	[7]
C3C1-C70	119.7×2.41	49.9×3.09	70.2	253.1	264.7	66.5	238.4	259.1	66.1	822.9	911.7	1.108	
C3C1-C100	119.3×2.45	49.9×3.10	106.0	253.1	264.7	66.5	238.4	259.1	66.1	1101.1	1199.2	1.089	
C3C2-C40	119.7×2.49	76.1×2.13	44.8	253.1	264.7	66.5	237.0	256	64.9	595.7	578.8	0.972	
C3C2-C70	119.6×2.50	76.1×2.05	70.2	253.1	264.7	66.5	237.0	256	64.9	701.0	708.6	1.011	
C3C2-C100	120.4×2.32	76.0×2.04	106.0	253.1	264.7	66.5	237.0	256	64.9	904.4	911.7	1.008	
C4C1-C40	149.9×2.50	50.0×3.17	44.8	267.9	282.9	64.9	238.4	259.1	66.1	1064.5	1043.4	0.980	
C4C1-C70	150.1×2.49	50.1×3.19	70.2	267.9	282.9	64.9	238.4	259.1	66.1	1438.7	1397.8	0.972	
C4C1-C100	150.0×2.50	50.0×3.13	106.0	267.9	282.9	64.9	238.4	259.1	66.1	1980.9	1898.1	0.958	
C4C2-C40	150.2×2.53	76.1×1.95	44.8	267.9	282.9	64.9	237.0	256	64.9	936.5	697.4	0.974	
C4C2-C70	150.0×2.51	75.9×2.08	70.2	267.9	282.9	64.9	237.0	256	64.9	1210.7	975.7	1.001	
C4C2-C100	149.8×2.54	76.1×2.02	106.0	267.9	282.9	64.9	237.0	256	64.9	1566.1	1437.5	1.026	
C5C1-C40	150.0×5.14	49.9×3.00	44.8	267.9	251.9	65.8	238.4	259.1	66.1	1465.8	1416.8	0.967	
C5C1-C70	150.3×4.98	50.0×3.07	70.2	267.9	251.9	65.8	238.4	259.1	66.1	1675.4	1708.5	1.020	
C5C1-C100	150.1×4.99	49.9×3.18	106.0	267.9	251.9	65.8	238.4	259.1	66.1	2095.0	2230.0	1.064	
C5C2-C40	150.2×4.94	76.0×2.09	44.8	267.9	251.9	65.8	237.0	256	64.9	1256.3	1213.0	0.975	
C5C2-C70	150.2×4.93	76.1×2.09	70.2	267.9	251.9	65.8	237.0	256	64.9	1368.0	1488.7	1.097	
C5C2-C100	150.3×4.94	76.1×2.12	106.0	267.9	251.9	65.8	237.0	256	64.9	1856.8	1886.7	1.023	
C6C1-C40	160.4×4.01	50.0×3.14	44.8	254.2	272.9	66.6	238.4	259.1	66.1	1373.3	1473.1	1.079	
C6C1-C70	160.5×4.02	50.0×3.15	70.2	254.2	272.9	66.6	238.4	259.1	66.1	1786.0	1890.3	1.064	
C6C1-C100	160.5×4.04	50.0×3.17	106.0	254.2	272.9	66.6	238.4	259.1	66.1	2540.0	2477.0	0.979	
C6C2-C40	160.5×4.02	76.1×2.02	44.8	254.2	272.9	66.6	237.0	256	64.9	1342.7	1295.0	0.971	
C6C2-C70	160.4×4.02	76.0×2.04	70.2	254.2	272.9	66.6	237.0	256	64.9	1472.3	1644.6	1.123	
C6C2-C100	160.7×4.02	76.1×2.00	106.0	254.2	272.9	66.6	237.0	256	64.9	2099.8	2137.1	1.022	
Mean												1.020	
Standard deviation (SD)												0.050	
Coefficient of variation (COV)												0.050	

Table 3 Lateral confining pressures on the sandwiched concrete confined by circular carbon steel tubes and aluminum tubes.

Specimens	$P_{u\exp}$ (kN)	Hu and Su model [36]			Proposed model Eq. (22)		
		f_{rp1} (MPa)	P_{ufrp1} (kN)	$\frac{P_{ufrp1}}{P_{u\exp}}$	f_{rp} (MPa)	P_{ufrp} (kN)	$\frac{P_{ufrp}}{P_{u\exp}}$
C3C1-C40	712.4	3.760	853.9	1.199	1.11	717.0	1.007
C3C1-C70	822.9	3.758	1055.0	1.282	1.05	911.7	1.108
C3C1-C100	1101.1	3.764	1338.3	1.215	1.09	1199.2	1.089
C3C2-C40	595.7	0.318	601.0	1.009	0.61	578.8	0.972
C3C2-C70	701.0	0	722.8	1.031	0.54	708.6	1.011
C3C2-C100	904.4	0.065	925.0	1.023	0.51	911.7	1.008
C4C1-C40	1064.5	3.882	1309.9	1.231	0.92	1043.4	0.980
C4C1-C70	1438.7	3.892	1674.0	1.164	0.93	1397.8	0.972
C4C1-C100	1980.9	3.876	2167.6	1.094	0.93	1898.1	0.958
C4C2-C40	936.5	0.049	915.8	0.978	0.60	697.4	0.974
C4C2-C70	1210.7	0.783	1250.9	1.033	0.71	975.7	1.001
C4C2-C100	1566.1	0.404	1621.0	1.035	0.64	1437.5	1.026
C5C1-C40	1465.8	4.268	1528.7	1.043	2.87	1416.8	0.967
C5C1-C70	1675.4	4.258	1848.5	1.103	2.74	1708.5	1.020
C5C1-C100	2095.0	4.329	2334.8	1.114	2.77	2230.0	1.064
C5C2-C40	1256.3	0	1173.7	0.934	1.67	1213.0	0.975
C5C2-C70	1368.0	0	1449.8	1.060	1.66	1488.7	1.097
C5C2-C100	1856.8	0	1845.8	0.994	1.70	1886.7	1.023
C6C1-C40	1373.3	3.914	1641.0	1.195	1.66	1473.1	1.079
C6C1-C70	1786.0	3.921	2058.4	1.153	1.67	1890.3	1.064
C6C1-C100	2540.0	3.935	2653.9	1.045	1.69	2477.0	0.979
C6C2-C40	1342.7	0	1276.6	0.951	0.81	1295.0	0.971
C6C2-C70	1472.3	0	1624.6	1.103	0.83	1644.6	1.123
C6C2-C100	2099.8	0	2120.1	1.010	0.78	2137.1	1.022
Mean				1.083			1.020
Standard deviation (SD)				0.094			0.050
Coefficient of variation (COV)				0.087			0.050

Table 4 Dimensions and material variables of circular DCFAT stub columns used in the parametric studies

Column	D_o (mm)	t_o (mm)	D_o/t_o	D_i (mm)	t_i (mm)	D_i/t_i	$\sigma_{0.2o}$, $\sigma_{0.2i}$ (MPa)	σ_{auo}, σ_{aui} (MPa)	f_c' (MPa)
C1	500	10	50	240	10	24.0	250	270	50
C2	600	10	60	180	7	25.7	250	260	40
C3	600	10	60	240	7	34.3	250	260	40
C4	600	10	60	300	7	42.9	250	260	40
C5	600	10	60	360	7	51.4	250	260	40
C6	450	10	45	200	6.67	30.0	270	280	65
C7	550	10	55	200	6.67	30.0	270	280	65
C8	600	10	60	200	6.67	30.0	270	280	65
C9	500	10	50	200	13.33	15.0	240	260	80
C10	500	10	50	200	8	25.0	240	260	80
C11	500	10	50	200	5.71	35.0	240	260	80
C12	700	14	50	350	10	35.0	220	250	100
C13	700	14	50	350	10	35.0	240	260	100
C14	700	14	50	350	10	35.0	250	260	100
C15	700	14	50	350	10	35.0	260	280	100
C16	550	10	55	250	10	25.0	250	260	40
C17	550	10	55	250	10	25.0	250	260	65
C18	550	10	55	250	10	25.0	250	260	80
C19	550	10	55	250	10	25.0	250	260	100
C20	300	6	50	150	5	30.0	270	280	65

Table 5 Comparison of experimental ultimate axial loads of DCFAT short columns with those calculated by the codified methods and design model.

Specimens	L (mm)	P_u (kN)	AISC 316-16 [54]		Eurocode 4 [55]		Liang [38]	
			$P_{u\text{AISC}}$ (kN)	$\frac{P_{u\text{AISC}}}{P_u}$	$P_{u\text{EC4}}$ (kN)	$\frac{P_{u\text{EC4}}}{P_u}$	$P_{u\text{Liang}}$ (kN)	$\frac{P_{u\text{Liang}}}{P_u}$
C3C1-C40	360	712.4	699.1	0.981	757.4	1.063	690.0	0.969
C3C1-C70	360	822.9	893.9	1.086	955.0	1.160	893.1	1.085
C3C1-C100	360	1101.1	1174.4	1.067	1243.2	1.129	1189.8	1.081
C3C2-C40	360	595.7	595.7	1.000	619.4	1.040	553.1	0.929
C3C2-C70	360	701.0	730.4	1.042	759.3	1.083	695.0	0.991
C3C2-C100	360	904.4	933.2	1.032	970.3	1.073	906.6	1.002
C4C1-C40	450	1064.5	1039.6	0.977	1142.2	1.073	1031.6	0.969
C4C1-C70	450	1438.7	1393.0	0.968	1502.5	1.044	1403.5	0.976
C4C1-C100	450	1980.9	1885.4	0.952	2008.8	1.014	1922.4	0.970
C4C2-C40	450	936.5	932.7	0.996	1010.6	1.079	893.3	0.954
C4C2-C70	450	1210.7	1225.1	1.012	1308.4	1.081	1204.0	0.994
C4C2-C100	450	1566.1	1624.6	1.037	1720.6	1.099	1622.1	1.036
C5C1-C40	450	1465.8	1182.1	0.806	1329.5	0.907	1337.5	0.912
C5C1-C70	450	1675.4	1501.7	0.896	1648.2	0.984	1663.3	0.993
C5C1-C100	450	2095.0	1960.6	0.936	2112.6	1.008	2147.0	1.025
C5C2-C40	450	1256.3	1069.1	0.851	1170.1	0.931	1126.2	0.896
C5C2-C70	449	1368.0	1331.5	0.973	1436.4	1.050	1401.6	1.025
C5C2-C100	450	1856.8	1707.5	0.920	1820.3	0.980	1799.0	0.969
C6C1-C40	480	1373.3	1303.6	0.949	1462.8	1.065	1370.9	0.998
C6C1-C70	480	1786.0	1699.4	0.952	1862.1	1.043	1788.1	1.001
C6C1-C100	480	2540.0	2255.6	0.888	2428.0	0.956	2375.0	0.935
C6C2-C40	480	1342.7	1197.2	0.892	1320.8	0.984	1191.8	0.888
C6C2-C70	480	1472.3	1527.7	1.038	1655.7	1.125	1541.0	1.047
C6C2-C100	480	2099.8	1998.5	0.952	2137.8	1.018	2034.1	0.969
C1	1500	11835.6	12101.4	1.004	12988.1	1.078	11614.8	0.964
C2	1800	13619.1	14657.9	1.035	16453.6	1.162	13914.7	0.982
C3	1800	13453.6	14235.7	1.038	15770.2	1.150	13385.7	0.976
C4	1800	13008.6	13598.5	1.095	14805.3	1.192	12156.8	0.979
C5	1800	12909.2	12746.5	1.090	13551.4	1.159	11400.7	0.975
C6	1350	11769.5	11853.4	1.012	12841.9	1.096	11668.8	0.996
C7	1650	16444.6	17357.5	1.047	18935.3	1.143	16534.6	0.998
C8	1800	18985.6	20473.3	1.056	22355.2	1.153	19374.5	0.999
C9	1500	16330.3	16935.7	1.010	18038.5	1.076	16439.2	0.981
C10	1500	15752.9	16217.7	1.014	17447.5	1.091	15854.3	0.992
C11	1500	15588.7	15896.0	1.037	17183.7	1.121	15431.7	1.007
C12	2100	32495.8	33541.6	1.049	35610.1	1.114	31958.4	0.999
C13	2100	33182.5	34358.7	1.055	36475.4	1.120	32615.9	1.001
C14	2100	33512.9	34767.2	1.058	36906.8	1.123	32944.7	1.003
C15	2100	33868.9	35175.7	1.061	37337.5	1.126	33273.4	1.004
C16	1650	12154.4	12644.3	1.017	13729.2	1.105	11915.8	0.959
C17	1650	16038.4	16718.1	1.025	17896.4	1.097	15987.0	0.980
C18	1650	18415.2	19162.5	1.025	20408.0	1.091	18429.8	0.985
C19	1650	21560.4	22421.5	1.027	23767.0	1.088	21686.8	0.993
C20	900	5026.1	5042.7	1.006	5385.8	1.074	4930.7	0.983
Mean				0.999		1.076		0.986
Standard deviation (SD)				0.063		0.064		0.039
Coefficient of variation (COV)				0.063		0.059		0.039

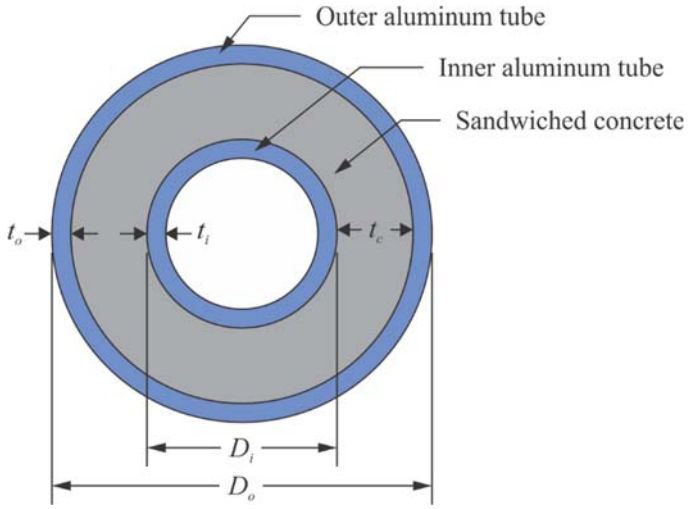

Fig. 1. Circular DCFAT column cross-section.

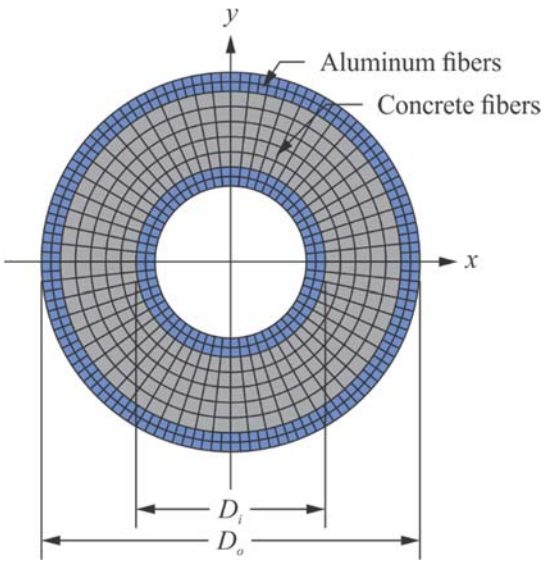

Fig. 2. Typical fiber mesh of circular DCFAT column.

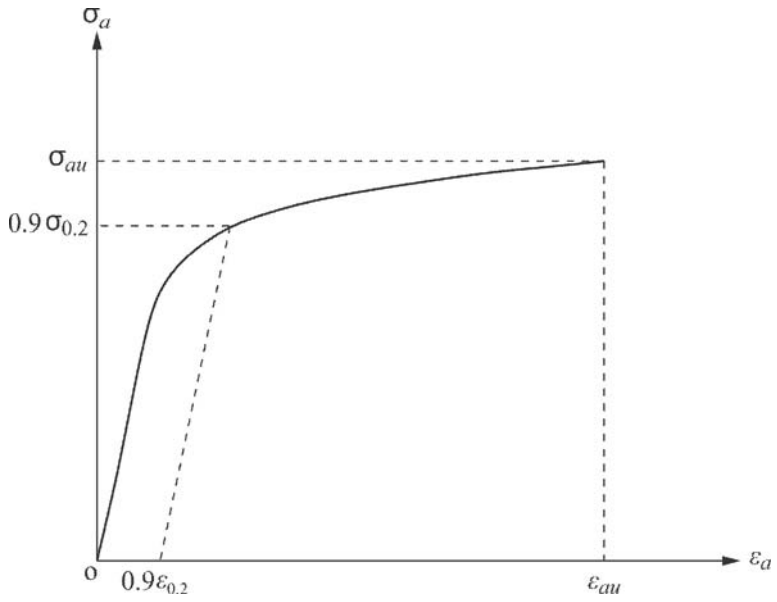

Fig. 3. Stress-strain curve for aluminum.

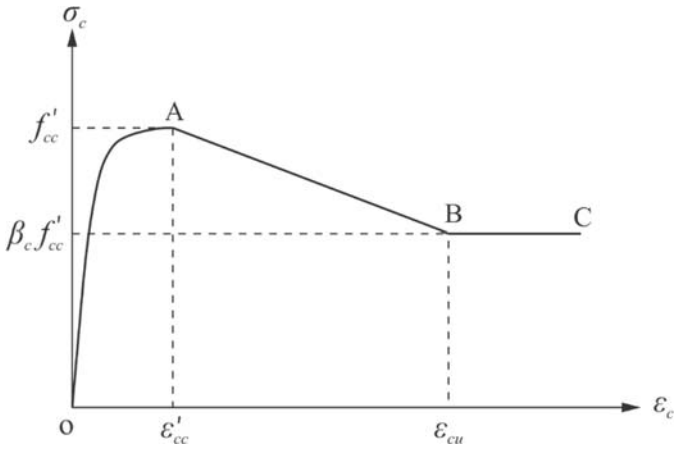

Fig. 4. Stress-strain curve for double-skin confined concrete.

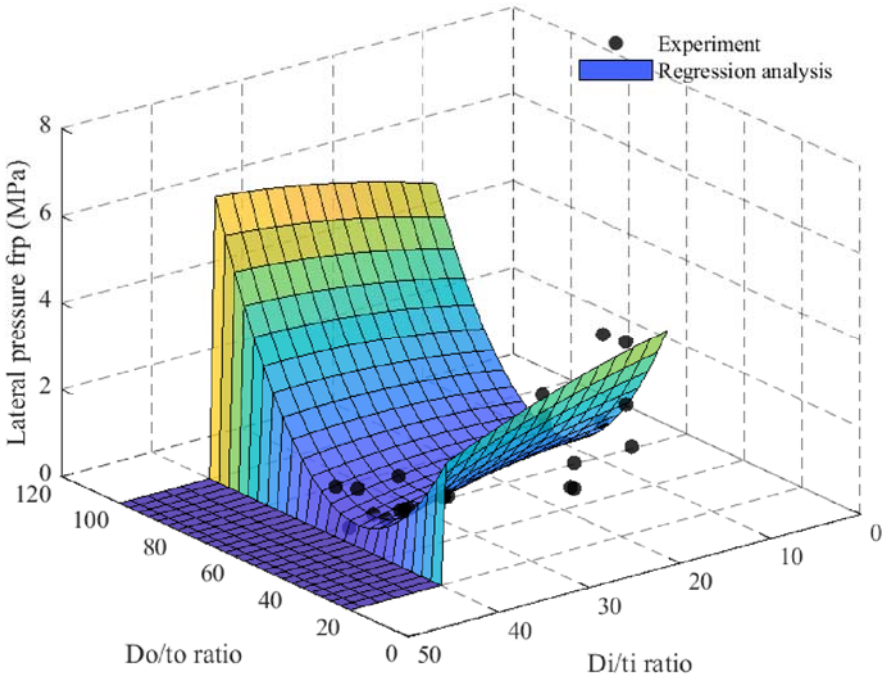

Fig. 5. Regression analysis for computing the lateral confining pressures from the experimental results [7].

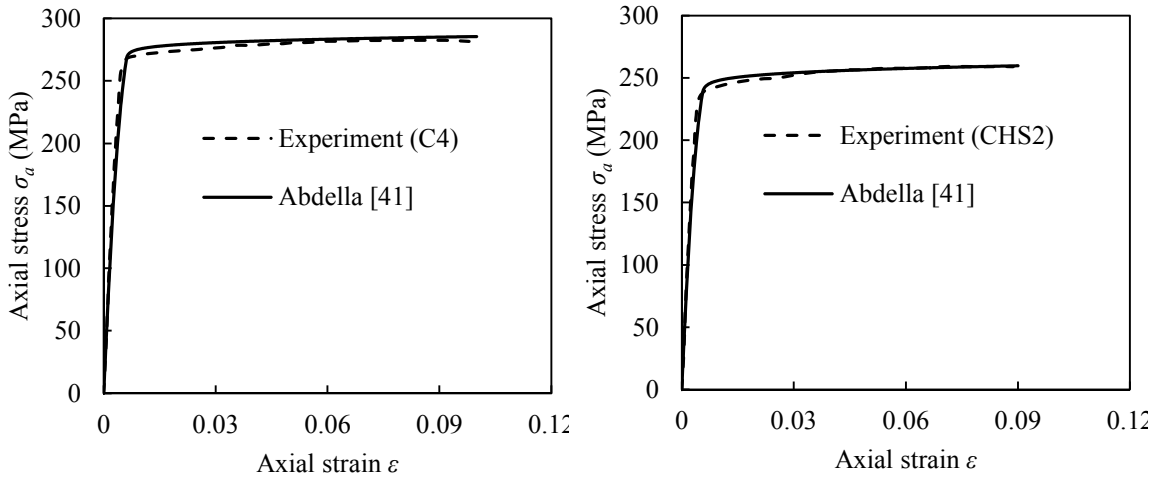

Fig. 6. Comparison of numerically captured and tested stress-strain responses of aluminum.

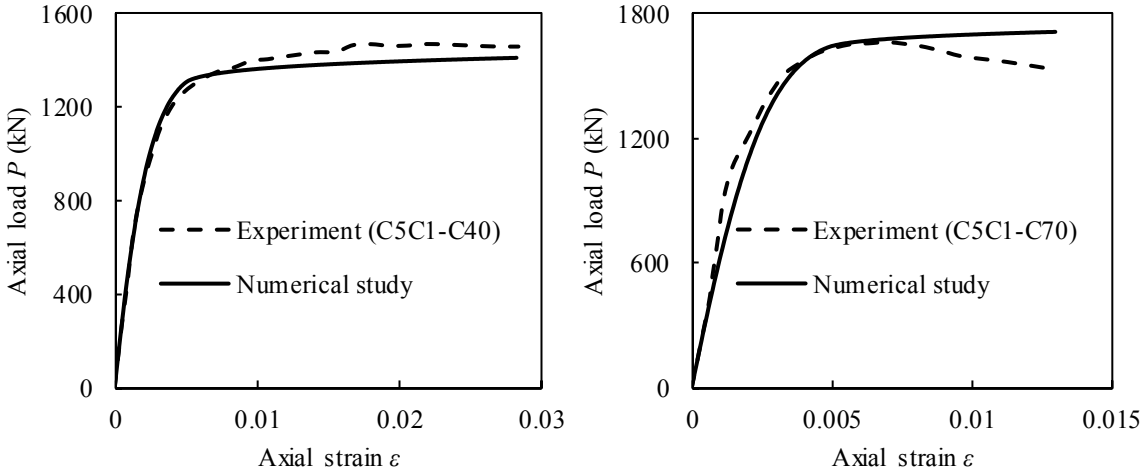

Fig. 7. Comparison of computed and experimental load-strain responses.

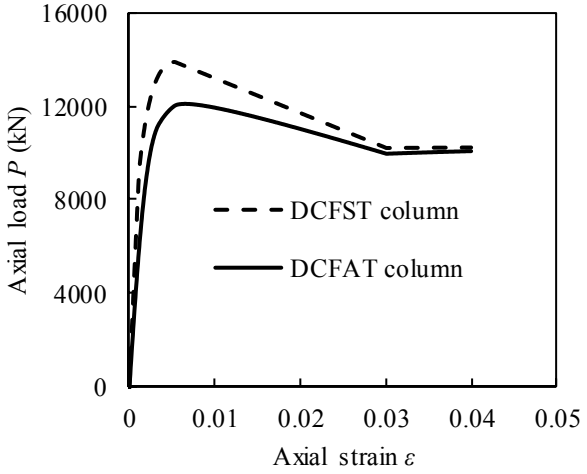

Fig. 8. Comparison of axial load-strain responses of circular DCFAT and DCFST columns.

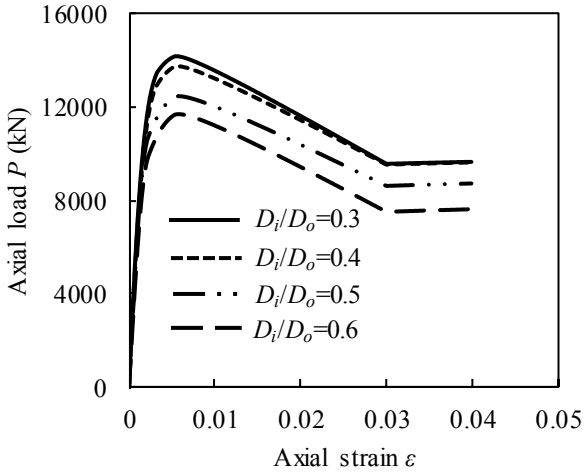

Fig. 9. Effect of D_i/D_o ratio on axial load-strain responses of circular DCFAT columns.

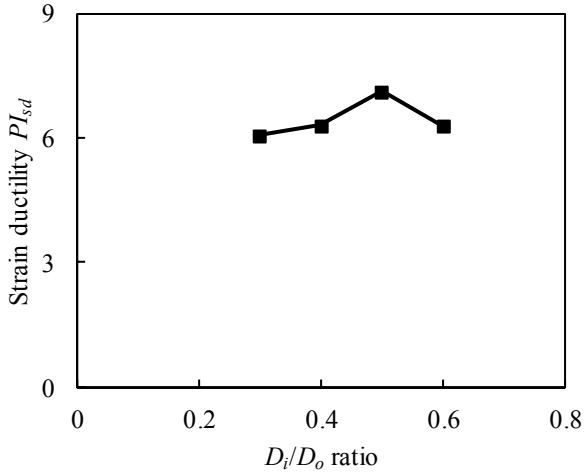

Fig. 10. Effect of D_i/D_o ratio on strain ductility PI_{sd}.

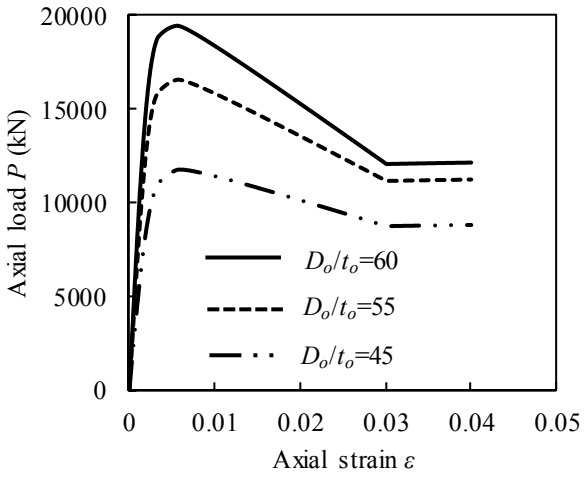

Fig. 11. Effect of D_o/t_o ratio on axial load-strain responses.

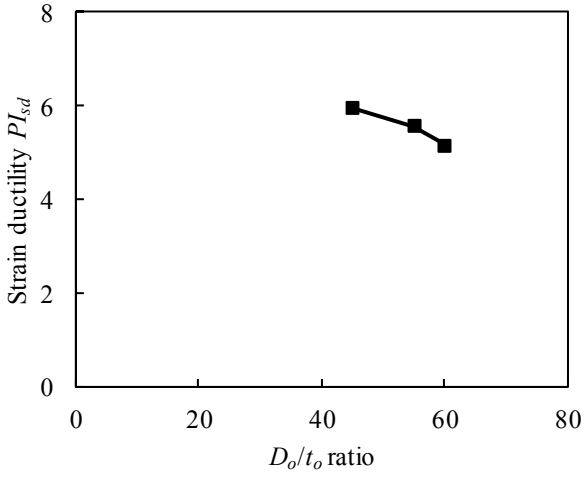

Fig. 12. Effect of D_o/t_o ratio on strain ductility PI_{sd}.

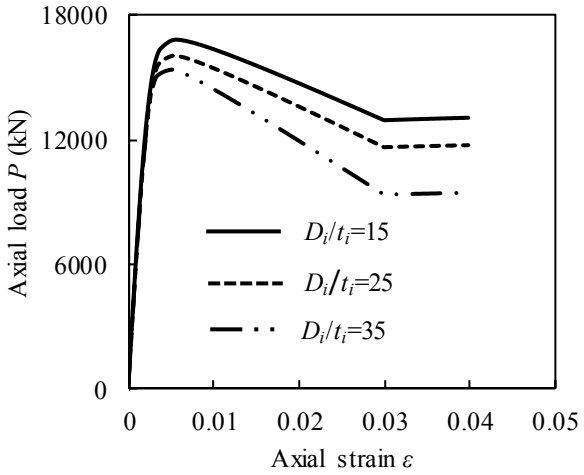

Fig. 13. Effect of D_i/t_i ratio on axial load-strain responses.

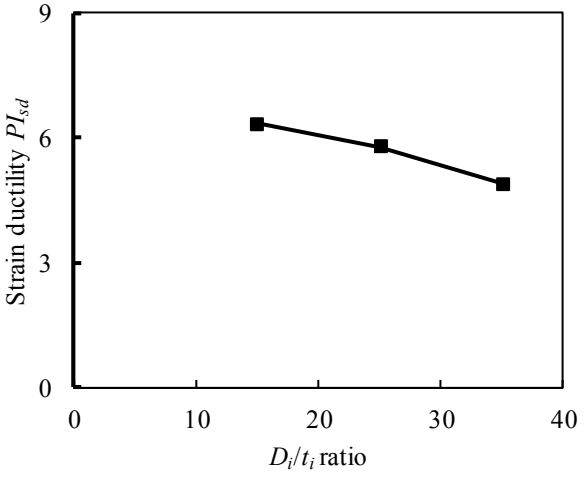

Fig. 14. Effect of D_i/t_i ratio on strain ductility PI_{sd}.

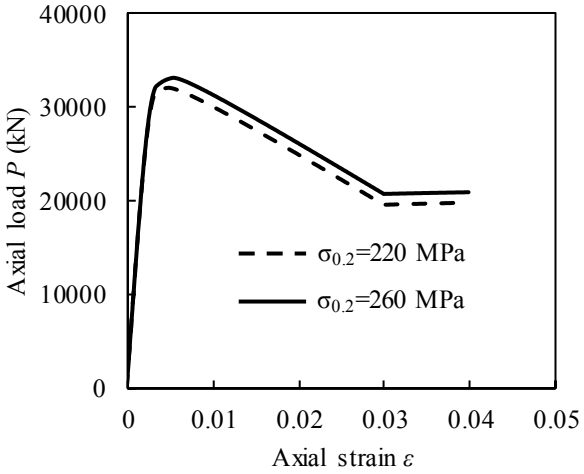

Fig. 15. Effect of aluminum strength on axial load-strain responses.

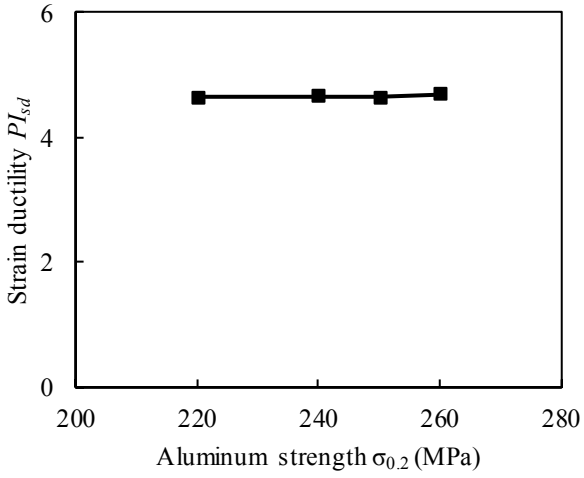

Fig. 16. Effect of aluminum strength on strain ductility PI_{sd} of circular DCFAT columns.

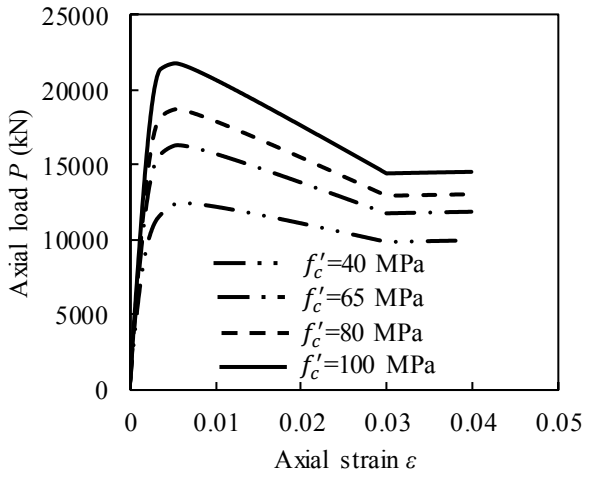

Fig. 17. Effect of concrete strength $f_c^{'}$ on load-strain responses.

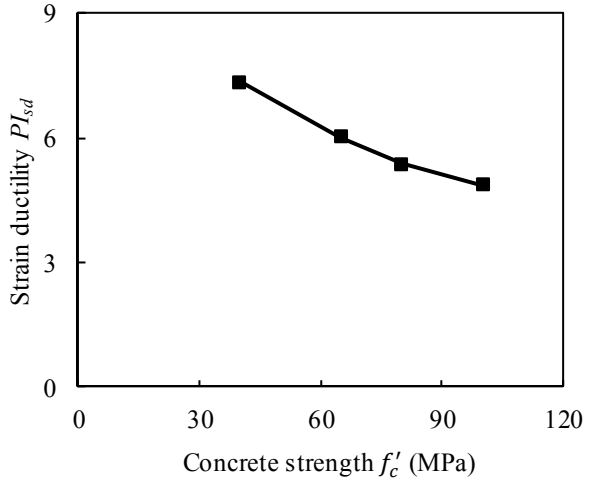

Fig. 18. Effect of concrete strength $f_c^{'}$ on strain ductility PI_{sd} of circular DCFAT columns.